

Characterizing X-ray properties of the gamma-ray pulsar PSR J1418–6058 in the Rabbit pulsar wind nebula

MINJUN KIM¹ AND HONGJUN AN¹

¹*Department of Astronomy and Space Science,
Chungbuk National University, Cheongju, 28644, Republic of Korea*

ABSTRACT

We report on X-ray studies of the gamma-ray pulsar PSR J1418–6058 in the Rabbit pulsar wind nebula (PWN) carried out using archival *Chandra* and *XMM-Newton* observations. A refined timing analysis performed with the 120-ks *XMM-Newton* data finds significant ($p \approx 10^{-7}$) pulsation at $P \approx 110$ ms which is consistent with that measured with the *Fermi* large area telescope (LAT). In the *Chandra* image, we find extended emission around the pulsar similar to those seen around other pulsars in young PWNe, which further argues for association between PSR J1418–6058 and the Rabbit PWN. The X-ray spectrum of the pulsar is hard and similar to those of soft-gamma pulsars. Hence PSR J1418–6058 may add to the list of soft-gamma pulsars.

Keywords: pulsars: individual (PSR J1418–6058) — stars: neutron — stars: winds, outflows — X-rays: general

1. INTRODUCTION

Pulsars, rapidly spinning neutron stars, are one of main sources of gamma-ray emission in the Galaxy, and so a large fraction of the *Fermi* large area telescope (LAT; Atwood et al. 2009) sources is pulsars. They are further categorized into several classes based on their temporal and spectral properties, from rapidly-spinning recycled pulsars to slowly-spinning hot magnetars (e.g., Harding 2013). Emission properties of pulsars are diverse; magnetars emit almost exclusively in the X-ray band (e.g., Kaspi & Beloborodov 2017), and recycled pulsars mainly do in the radio and the gamma-ray bands. Some relatively young pulsars emit nonthermal radiation in the X-ray band which becomes softer at gamma-ray energies (Kuiper & Hermsen 2015). Pulsars’ timing properties are also various; the spin periods range from milliseconds to tens of seconds, and some pulsars exhibit frequent timing anomaly (e.g., glitches) while others do not. These observational diversities can be explained with the fundamental neutron star physics to some degrees, but more studies are needed to understand them better. In addition, characterizing pulsar properties is important to understand pulsar wind nebulae (PWNe) with which we can study the relativistic

shock physics (Sironi et al. 2015) and magnetohydrodynamic flow of high-energy particles (Kennel & Coroniti 1984),

Observational studies of pulsars are mainly done in the radio, X-ray and gamma-ray bands (e.g., Coti Zelati et al. 2019) because pulsars are bright in these bands. Energetic gamma-ray pulsars are often discovered by *Fermi*-LAT blind searches which are later confirmed by observations in other wavebands. While continuous monitoring of the sky by *Fermi* LAT allowed precise measurements of pulsars’ spin properties (Abdo et al. 2013), it is difficult to characterize their short-timescale properties due to low count statistics in the gamma-ray band. These can be measured better in the other wavebands, but identifying a low-energy counterpart of a gamma-ray pulsar based on the position is difficult due to insufficient angular resolution of gamma-ray telescopes; there can be several X-ray point sources in the LAT-determined position error circle. However, it was shown that *Fermi* timing analyses could determine pulsars’ position to high precision (to the arcsecond level), which has been verified by previous studies (e.g., Kerr et al. 2015).

The pulsar PSR J1418–6058 was first identified as a bright gamma-ray source by *EGRET* (Lamb & Macomb 1997). Follow-up radio and X-ray studies found complex structure (Kookaburra region) around the source, most importantly an extended radio and X-ray PWN (“Rabbit”; Roberts et al. 1999). Interestingly extended TeV

Corresponding author: Hongjun An
hjan@cbnu.ac.kr

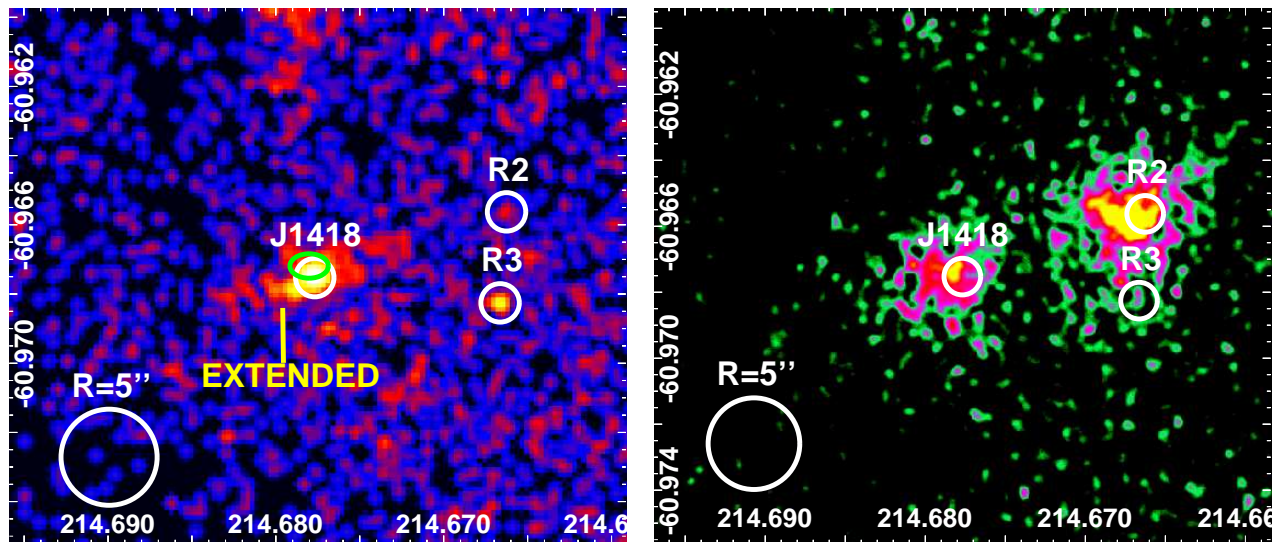


Figure 1. 1–10 keV *Chandra* (left) and *XMM-Newton* Mos-combined (right) images of $\sim 1' \times 1'$ regions around J1418. Some sources are denoted with circles ($R = 2''$), and an $R = 5''$ circle is shown in the bottom left corner for reference. The green ellipse denotes the LAT-timing position of PSR J1418–6058 (Kerr et al. 2015), and extended emission around J1418 is clearly visible in the left panel. Figures are smoothed and scales are adjusted for better legibility.

emission was detected near the PWN (Aharonian et al. 2006) and suggested to be associated with it. However, it was unclear whether PSR J1418–6058 is associated with the PWN because there are multiple X-ray sources in the region (Fig. 1; see also Ng et al. 2005), and X-ray pulsation was not detected significantly in any of them. Subsequent timing studies with *Fermi* LAT discovered a pulsar and allowed high-precision astrometry for the pulsar position (green circle in Fig. 1 left; Kerr et al. 2015) which is consistent with the position of an X-ray source. Hence the source (J1418 hereafter) is likely to be the X-ray counterpart of PSR J1418–6058. Further X-ray studies will then help to measure timing properties on short timescales and understand the nature of the pulsar.

Moreover, if J1418 is associated with the Rabbit PWN, characterizing J1418’s properties can help to understand the intriguing PWN having the TeV emission offset from the radio and X-ray one; by modeling the X-ray and gamma-ray light curves of the pulsar (Harding & Muslimov 1998; Romani & Watters 2010) and the torus morphology (Ng & Romani 2004), the pulsar emission geometry can be inferred, which can then tell us about its energy injection to the PWN.

In this paper, we investigate temporal, spectral, and spatial properties of X-ray sources in the Rabbit PWN to identify unambiguously the central pulsar (likely J1418) and to measure its properties using archival *Chandra* and *XMM-Newton* data.

2. OBSERVATIONAL DATA AND ANALYSIS

2.1. Data reduction

We use archival X-ray data obtained with the *Chandra* and the *XMM-Newton* satellites. The data were taken on 2007 June 14 for 70 ks (Obs. ID 7640) and on 2009 Feb. 21 for 120 ks (Obs. ID 0555700101, MJD 54883) with *Chandra* and *XMM-Newton*, respectively. These data were reduced with the pipeline tools along with the most recent calibration database for each observatory: CIAO 4.11 and SAS 20180620. We processed the *Chandra* data using the `chandra_repro` task and the *XMM-Newton* data using the `emproc` and `epproc` tasks with standard filters. We further cleaned the *XMM-Newton* data to remove particle-flare events using the standard flare-removal procedure.¹

2.2. X-ray timing analysis

We first search the X-ray data for pulsations (e.g., $P=110$ ms) of sources in the Rabbit PWN. This can be done only with the *XMM-Newton*/PN small-window mode observation with sufficient timing resolution ($\Delta T = 5.7$ ms; for a detection of the 110 ms pulsation). In the *XMM-Newton*/PN data, we find two bright sources $\sim 20''$ away from each other (Fig. 1 right); one of them (the eastern one; J1418) is positionally coincident with the gamma-ray pulsar PSR J1418–6058 (green circle in the left panel). Note that the point source denoted as R3 in the left panel (*Chandra* data) is not present in the right panel (*XMM-Newton* data).

¹ <https://www.cosmos.esa.int/web/xmm-newton/sas-thread-epic-filterbackground>

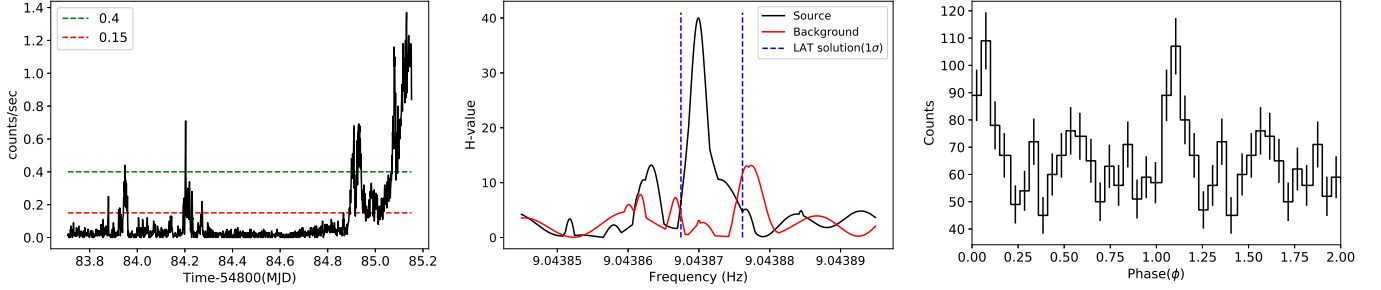


Figure 2. *Left:* A particle-flare light curve measured with the *XMM-Newton* PN data. Horizontal lines denote the flare filtering criteria: a standard cut 0.4 s^{-1} (green) and a tight cut 0.15 s^{-1} (red). *Middle:* H -test results for the source (black) events in the 1–10 keV band, with the flare cut of 0.15 s^{-1} . Results for the background events (an $R = 30''$ circle) are also shown in red and the 1σ range of the LAT solution at the X-ray epoch is shown in blue for reference. *Right:* A 1–10 keV pulse profile (flare cut 0.15 s^{-1}) constructed by folding the source events on the best period (Section 2.2).

We extract 1–10 keV events within $10''$ circles centered at the positions of the two X-ray sources (J1418 and R2), and barycenter-correct the event arrival times using (R.A., decl.)=(214.677695°, -60.967483°) and (214.667428°, -60.965500°) for the eastern (J1418) and the western (R2) source, respectively. We produce and inspect the light curves of the sources, and find some flares. We suspect that the standard flare-filtering ($\leq 0.4 \text{ s}^{-1}$) leaves a large number of particle-flare events unfiltered (Fig. 2 left). This may be a concern for timing studies because backgrounds cannot be directly subtracted in timing analyses (e.g., Fourier analysis and epoch-folding techniques). We therefore inspect the flare light curve (Fig. 2 left), and find that we can better remove the flare backgrounds by adjusting the flare cut to a lower value.

After visual inspection of the flare light curve, we change the flare cut to $\leq 0.15 \text{ s}^{-1}$ (see below for different cuts). This reduces the number of events in the source region of J1418 by $\approx 30\%$. We then fold the event arrival times using the *Fermi*-LAT timing solution (Kerr et al. 2015) and find that pulsation of J1418 is detected significantly ($p = 2 \times 10^{-7}$ for $H = 39$) but not for R2; the folded X-ray pulse profile of J1418 shows a sharp peak at $\phi \approx 0.1$ and another smaller (and less clear) one at $\phi \approx 0.6$, similar to that in Figure 2 right and a previously-reported one.² These peak phases are similar to those of the GeV peaks.³

We further check to see if the results change significantly when using different event selections: energy band, source region, or flare cut (Table 1). The H value for the pulsation varies between 25 and 46 ($p = 4 \times 10^{-5} - 9 \times 10^{-9}$) when varying the energy band (e.g., lower bound 0.5–1.5 keV and upper bound 6–10 keV), source-

Table 1. Detection significance of the pulsation for various event selections

Flare cut	Energy band (keV)	Region shift ($''/''$) ^a	H -value	Cts/Exposure (/ks)
0.03	1–10	0/0	32.07	741/48
0.07	1–10	0/0	40.50	1064/64
0.1	1–10	0/0	46.26	1130/67
0.2	1–10	0/0	43.92	1430/74
0.3	1–10	0/0	40.05	1720/79
0.4	1–10	0/0	36.41	1830/81
0.15	0.5–10	0/0	36.06	1370/71
0.15	1–10	0/0	38.69	1300/71
0.15	1.5–10	0/0	33.68	1200/71
0.15	1–8	0/0	38.48	1210/71
0.15	1–6	0/0	32.25	1036/71
0.15	1–10	3/0	41.25	1290/71
0.15	1–10	$-3/0$	28.22	1320/71
0.15	1–10	0/3	25.28	1290/71
0.15	1–10	0/ -3	43.65	1280/71

^aR.A./Decl.

region center (by $3''$ in all directions), or the flare cut value (0.03–0.4); the detection becomes less significant (lower H values) for source regions that are close to R2, narrower energy bands or non-optimal flare-cut values. Nevertheless, all of these selections result in a significant detection, and hence the detection of the pulsation in J1418 is robust. However, we note that using a large region (e.g., $R > 20''$) and/or a narrower energy range (e.g., 3–9 keV) reduces the signal-to-noise ratio and makes the detection insignificant.

Because the LAT timing solution was constructed by using large time bins compared to the exposure of the X-ray data, the solution may not properly account for timing noise effects at the epoch of the X-ray observation and hence may not be optimal. We therefore try to find a better frequency by carrying out H tests (de Jager et al. 1989) near the LAT solution $f = 9.0438674 - 9.0438762 \text{ s}^{-1}$ and find a sharp peak in the H plot (Fig. 2 middle) at $f = 9.0438699 \text{ s}^{-1}$ with

² https://cxc.harvard.edu/cdo/snr09/pres/Roberts_Mallory.pdf

³ https://www.slac.stanford.edu/~kerrm/fermi_pulsar_timing/

$H = 40$ (reference epoch MJD 54883), corresponding to $p = 1 \times 10^{-7}$. This result is robust to a small change of event selection (energy band, region, or flare cut) Note that we cannot determine frequency derivatives because of the low count statistics. The resulting pulse profile is displayed in Figure 2 right.

2.3. The pulsar spectral analyses

J1418 was suggested to be a soft-gamma pulsar candidate (Kuiper & Hermsen 2015), and then its X-ray spectrum is presumably hard. Now that we clearly identified it as a pulsar, we are able to measure its pulsed spectrum as well as phase-summed one.

For a phase-summed spectral analysis, *XMM-Newton* data (both MOS and PN) are not very useful because the pulsar is relatively faint and so contamination from emission of the bright surrounding region (e.g., R2 in Fig. 1 right) is a concern. We therefore use only the high spatial-resolution *Chandra* data for the phase-summed spectral analysis. We extract source events within an $R = 2''$ circle and background events using an $R = 2.1 - 5''$ annular region; the latter is selected so as to properly take into account backgrounds from the possible extended emission (Fig. 1 and Section 2.4). Corresponding response files are calculated with the `spec_extract` tool of CIAO. We group the spectrum to have at least 5 events in each spectral bin, fit the 0.5–10 keV spectrum with an absorbed power-law model in XSPEC V12.10.1 employing *lstat* (Loredo 1992) because of paucity of counts. We find that the power-law model with $N_{\text{H}} = 2.8 \pm 0.7 \times 10^{22} \text{ cm}^{-2}$, $\Gamma = 1.5 \pm 0.4$, and 0.5–10 keV flux $F_{\text{X}} = 1.5 \pm 0.3 \times 10^{-13} \text{ erg cm}^{-2} \text{ s}^{-1}$ adequately describes the data (*lstat/dof*=31/41). The results are summarized in Table 2. A blackbody model also explains the data but the best-fit temperature appears to be too high ($kT = 1.5 \text{ keV}$). So we do not report the results. Note that these results obtained with the 70-ks *Chandra* data are qualitatively similar to those reported by Ng et al. (2005) based on 10-ks *Chandra* and 25-ks *XMM-Newton* data, but quantitative comparison is not possible because detailed information on the analysis is missing in that work.

We next measure the pulsed-spectrum using the *XMM-newton*/PN data. Although there is a *Fermi-LAT* timing solution, we use our own solution because the LAT solution was constructed by using relatively large time bins and may not adequately account for timing noise with the timescale of the 120-ks *XMM-newton* exposure. The pulse profile seems to consist of two peaks around $\phi = 0.1$ and 0.6, but the second peak is less significant (Fig. 2 right). We therefore focus on the first peak here. We select phase intervals of

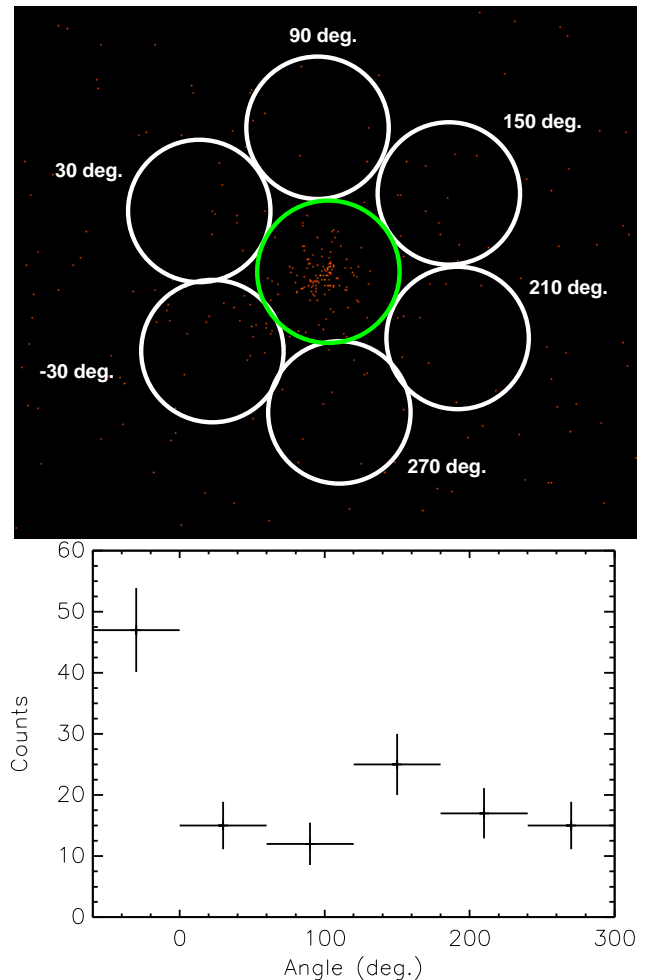


Figure 3. *Top:* A 1–10 keV *Chandra* image of J1418 vicinity with regions surrounding the pulsar (green circle). *Bottom:* Numbers of events contained within $R = 2''$ circles (white circles in the top panel). The angle is defined from east to north.

$\phi = 0 - 0.2$ and $\phi = 0.2 - 1.0$ for the pulsed spectrum and the unpulsed background, respectively. We extract the spectra using an $R = 10''$ circular region in the *XMM-Newton*/PN data, and compute the response files using the `rmfgen` and the `arfgen` tasks of SAS. We group the pulsed spectrum to have at least 5 events per bin and fit the 0.5–10 keV spectrum with an absorbed power law holding N_{H} fixed at the *Chandra*-measured value for the phase-summed spectrum. The model describes the spectrum well (*lstat/dof*=54/66) with $\Gamma = 1.0 \pm 0.6$ and the 0.5–10 keV flux $F_{\text{X}} = 1.3 \pm 0.3 \times 10^{-13} \text{ erg cm}^{-2} \text{ s}^{-1}$.

2.4. Image analysis

We inspect multi-epoch images obtained with the *Chandra* and *XMM-Newton* observations. Figure 1 shows 0.5–10 keV *Chandra* and *XMM-Newton* images of the field. In these images, we find that J1418 is persistently detected. However, the source R3 in the *Chan-*

Table 2. Power-law fit results for the pulsar and the extended emission

Data	Instrument	Energy range (keV)	N_{H} (10^{22} cm $^{-2}$)	Γ	F_{X} (10^{-13} erg s $^{-1}$ cm $^{-2}$)	$lstat/dof$
PSR phase summed	<i>Chandra</i>	0.5–10	2.8 ± 0.7	1.5 ± 0.4	1.5 ± 0.3	31/41
PSR pulsed	<i>XMM/</i> PN	0.5–10	2.8^{a}	1.0 ± 0.6	1.3 ± 0.3	54/66
Extended emission	<i>Chandra</i>	0.5–10	2.8^{a}	1.8 ± 0.3	0.7 ± 0.1	23/16

^aFixed at the value measured for the phase-summed spectrum.

dra image is not present in the *XMM-Newton* data. Instead, another source R2 is detected at $\sim 10''$ north to R3, meaning that these two sources R2 and R3 are variable. Note that considering agreement between *Chandra* and *XMM-Newton* positions of other sources in the field, this is not due to the positional inaccuracy of the observatories. Since R2 and R3 are highly variable, they are not likely to be a pulsar.

Focusing on J1418, we find extended emission around it in the south-east to north-west direction ($\approx 5''$; Fig. 1 left and Fig. 3) with the eastern part being slightly brighter. In order to verify this, we count the number of 1–10 keV events within six $R = 2''$ circles surrounding the J1418 region (Fig. 3 top), and show the angular distribution of the counts in Figure 3 bottom. The angle (θ) is defined from east to north, so that the $\theta \approx -30^\circ$ zone corresponds to the south-east region. This region contains 47 ± 7 events as compared to 17 ± 2 , the average of the other regions; the difference is 4.7σ significant. The north-west region ($\theta = 150^\circ$) also seems to have more counts than the other four lower-count zones (2σ significant). A formal χ^2 test rules out a flat distribution with $p = 2 \times 10^{-5}$.

We confirm the source extendedness using the `srcextent` tool of CIAO. We generate point source events (i.e., point spread function; PSF) using a *MARX* simulation⁴ appropriate to the observation parameters and the source spectrum we measured (Table 2). We then run the `srcextent` script with the observed event and the simulated PSF files on various spatial scales $R = 2 - 10''$, and find that the source is extended at 90% confidence for $R \geq 3''$ scales. At $R < 3''$, the event distribution is not significantly different from the PSF at the 90% confidence level. We also check to see if the extended emission is produced by a faint source adjacent to J1418 using the source detection tool `wavdetect` of CIAO. It properly detects nearby point sources (e.g., R3 in Fig. 1), but none in the region surrounding J1418. Hence the extended emission seems not to arise from a faint point source.

In order to measure the spectrum of the extended emission, we extract source events within a $3'' \times 5''$ ellipse

excluding the central $R = 2''$ region, and background events within a $R = 50''$ circle $2.5'$ north to the pulsar. Response files for the extended emission are generated with the `spec_extract` tool of CIAO. We group the source spectrum to have at least 5 events per spectral bin and fit the spectrum with an absorbed power-law model holding N_{H} fixed at 2.8×10^{22} cm $^{-2}$. The power-law model describes the spectrum well ($lstat/dof=23/16$) having $\Gamma = 1.8 \pm 0.3$ and 0.5–10 keV flux $F_{\text{X}} = 7 \pm 1 \times 10^{-14}$ erg cm $^{-2}$ s $^{-1}$ (Table 2).

3. DISCUSSION AND CONCLUSIONS

We found significant X-ray pulsation of J1418 in the Rabbit PWN, thereby confirming that J1418 is the X-ray counterpart of the gamma-ray pulsar PSR J1418–6058. Our image analysis revealed extended emission around the pulsar in the south-east to north-west direction with a position angle 30° from west to north. The extended emission may be a torus or jets often seen around pulsars in young PWNe. We note that similar and qualitative results were reported previously.⁵ We also find that the other X-ray sources in the Rabbit PWN are variable and hence are not pulsars. These findings strongly suggest that J1418 is the power source of the Rabbit PWN. The pulsar’s X-ray spectra appear to be hard with $\Gamma \approx 1$ similar to other soft-gamma pulsars.

The *XMM-Newton*/PN small-window data provide sufficient timing resolution to search for the 110 ms pulsation of J1418. Searches for its X-ray pulsation were attempted in the past with the same *XMM-Newton*/PN data, but the pulsation was not significantly detected (e.g., Kuiper & Hermsen 2015). This is probably because they used a large region ($R = 15''$), narrow energy bands (0.3–2 keV or 2–10 keV), and/or the standard flare cut (≤ 0.4 s $^{-1}$). Here we showed that optimizing the event selection in *XMM-Newton* data analyses can increase sensitivity for pulsation search and result in a significant detection.

In the high-resolution *Chandra* image, we found extended emission around J1418. Similar features are seen in young X-ray bright PWNe and interpreted as

⁴ <https://space.mit.edu/cxc/marx/>

⁵ https://cxc.harvard.edu/cdo/snr09/pres/Roberts_Mallory.pdf

a torus corresponding to termination shock or bipolar jets (e.g., Crab, MSH 15–52, and 3C 58; Madsen et al. 2015; An et al. 2014; Slane et al. 2004). Although it is not clear whether the extended emission around J1418 is jets or a torus, the emission is brighter in the eastern side, which could be due to the Doppler boosting (Ng & Romani 2004) of collimated bipolar outflow, suggesting that the feature perhaps corresponds to jets. If so, we can estimate the jet viewing angle to be $\zeta = 67^\circ$ for the jet-to-counterjet count ratio of ~ 3 (Fig. 3 bottom) and the photon index $\Gamma = 1.8$ (Table 2), using a Doppler boost formula (e.g., Ng & Romani 2004) for an assumed bulk flow speed of $\beta_{\text{jet}} = 0.5$. Further confirmation can be made by comparing the pulsar emission geometry inferred from gamma-ray profile fitting (Harding & Muslimov 1998; Romani & Watters 2010) with that inferred from torus fitting (e.g., Ng & Romani 2004).

The timing properties of J1418, spin-down luminosity $L_{\text{sd}} = 5 \times 10^{36}$ erg s $^{-1}$, the characteristic age $\tau_c = 10$ kyr, and the magnetic-field strength $B_s = 4 \times 10^{12}$ G (Kerr et al. 2015), are within the ranges for those of soft-gamma pulsars. Hence, the source was suggested to be a soft-gamma pulsar candidate previously (Kuiper & Hermsen 2015). We found that the X-ray spectra of the pulsar are hard similar to those of soft-gamma pulsars ($\Gamma_X \approx 1$), confirming the previous sug-

gestion. Hence J1418 may add to the list of soft-gamma pulsars.

With the current data, it is hard to measure properties of J1418 well. Accurate measurements of the X-ray pulse profile and spectra can help to understand the pulsar and the Rabbit PWN. In particular, identifying the extended emission as a torus or jets can be useful for understanding the energy injection to the Rabbit PWN. Since the pulsar has hard X-ray spectra, *NuSTAR* (Harrison et al. 2013) observations can easily detect the pulsations (e.g., as in PSR J0205+6449; An 2019) and characterize the pulse profile and emission spectrum. So further studies with *NuSTAR* are warranted.

We thank Matthew Kerr for discussions on the timing works. This research was supported by Basic Science Research Program through the National Research Foundation of Korea (NRF) funded by the Ministry of Science, ICT & Future Planning (NRF-2017R1C1B2004566).

Facilities: CXO, XMM

Software: HEASoft (v6.24; HEASARC 2014), CIAO (v4.11; Fruscione et al. 2006), XMM-SAS (v20180620; Gabriel 2017), XSPEC (Arnaud 1996)

REFERENCES

- Abdo, A. A., Ajello, M., Allafort, A., et al. 2013, *ApJS*, 208, 17
- Aharonian, F., Akhperjanian, A. G., Bazer-Bachi, A. R., et al. 2006, *A&A*, 456, 245
- An, H. 2019, *ApJ*, 876, 150
- An, H., Madsen, K. K., Reynolds, S. P., et al. 2014, *ApJ*, 793, 90
- Arnaud, K. A. 1996, in *Astronomical Society of the Pacific Conference Series*, Vol. 101, *Astronomical Data Analysis Software and Systems V*, ed. G. H. Jacoby & J. Barnes, 17
- Atwood, W. B., Abdo, A. A., Ackermann, M., et al. 2009, *ApJ*, 697, 1071
- Coti Zelati, F., Torres, D. F., Li, J., & Viganò, D. 2019, arXiv e-prints, arXiv:1912.03953
- de Jager, O. C., Raubenheimer, B. C., & Swanepoel, J. W. H. 1989, *A&A*, 221, 180
- Fruscione, A., McDowell, J. C., Allen, G. E., et al. 2006, in *Proc. SPIE*, Vol. 6270, *Society of Photo-Optical Instrumentation Engineers (SPIE) Conference Series*, 62701V
- Gabriel, C. 2017, in *The X-ray Universe 2017*, 84
- Harding, A. K. 2013, *Frontiers of Physics*, 8, 679
- Harding, A. K., & Muslimov, A. G. 1998, *ApJ*, 500, 862
- Harrison, F. A., Craig, W. W., Christensen, F. E., et al. 2013, *ApJ*, 770, 103
- Kaspi, V. M., & Beloborodov, A. M. 2017, *ARA&A*, 55, 261
- Kennel, C. F., & Coroniti, F. V. 1984, *ApJ*, 283, 694
- Kerr, M., Ray, P. S., Johnston, S., Shannon, R. M., & Camilo, F. 2015, *ApJ*, 814, 128
- Kuiper, L., & Hermsen, W. 2015, *MNRAS*, 449, 3827
- Lamb, R. C., & Macomb, D. J. 1997, *ApJ*, 488, 872
- Loredò, T. J. 1992, in *Statistical Challenges in Modern Astronomy*, ed. E. D. Feigelson & G. J. Babu, 275–297
- Madsen, K. K., Reynolds, S., Harrison, F., et al. 2015, *ApJ*, 801, 66
- Ng, C. Y., Roberts, M. S. E., & Romani, R. W. 2005, *ApJ*, 627, 904
- Ng, C. Y., & Romani, R. W. 2004, *ApJ*, 601, 479
- Roberts, M. S. E., Romani, R. W., Johnston, S., & Green, A. J. 1999, *ApJ*, 515, 712

Romani, R. W., & Watters, K. P. 2010, ApJ, 714, 810

Sironi, L., Keshet, U., & Lemoine, M. 2015, SSRv, 191, 519

Slane, P., Helfand, D. J., van der Swaluw, E., & Murray,
S. S. 2004, ApJ, 616, 403